IEEE Open Journal of the
Industrial Electronics Society

Received 20 September 2024; accepted 16 October 2024. Date of publication 28 October 2024; date of current version 11 November 2024. The review of this article was arranged by Associate Editor Thomas I. Strasser.

Digital Object Identifier 10.1109/OJIES.2024.3486560

Short-Term Control of Heat Pumps to Support Power Grid Operation

DIRAN LIU [1,2] (Member, IEEE), DANIELE CARTA [1] (Member, IEEE), ANDRÉ XHONNEUX[1], DIRK MÜLLER[1,2,3], AND ANDREA BENIGNI [1,2,3] (Senior Member, IEEE)

[1] ICE-1: Energy Systems Engineering, Forschungszentrum Jülich, 52428 Jülich, Germany
[2] RWTH Aachen University, 52056 Aachen, Germany
[3] JARA-Energy, 52425 Jülich, Germany

CORRESPONDING AUTHOR: DIRAN LIU (e-mail: d.liu@fz-juelich.de).

This work was supported by the European Commission Horizon Europe Programme under Grant 101096511.

ABSTRACT The increasing adoption of heat pumps presents new challenges for power grids, including the potential overloading of transformers and cables. To address this issue, in this work, a model predictive control for a low-temperature district heating network is proposed to prevent the overloading of transformers and cables. A comprehensive control strategy that considers various factors influencing the flexibility of heat pumps is introduced. The considered factors include integrating distributed energy resources (DER) such as a photovoltaic system, a battery energy storage system, and flexible indoor temperatures. The control mechanism is validated through a hardware-in-the-loop cosimulation setup, ensuring practical applicability and operational feasibility. The results indicate that with the proposed control, the power consumption of the heat pumps is reduced to alleviate overloading issues. To meet the power consumption constraints imposed on the heat pumps the gas usage by the heating grid would increase up to 506% of the level in the case without power constraints. However, by integrating DERs, along with leveraging the flexibility in indoor temperature, this additional gas usage is limited to 135%.

INDEX TERMS Model predictive control, LTDH network, distribution grid, hardware-in-the-loop, cosimulation.

I. INTRODUCTION

The widespread electrification of the heating sector-through the integration of renewable energies [1]—is essential to reduce Greenhouse gas emissions. However, this can also pose challenges for the power grid. The electrification is exemplified by the growing penetration of heat pumps in heating systems, promoted by their low carbon emissions, which consequently contributes to increasing the grid load [2]. However, the inherent thermal storage and inertia properties of heating systems offer an opportunity to develop flexible operational strategies for heat pumps. These strategies are not only crucial in preventing grid overloads but are also in reducing investment costs for upgrading grid infrastructure, e.g., for transformers and cables.

The potential of heat pumps to support power grid management through flexible operation has attracted considerable interest in the research community [3], [4]. Model Predictive Control (MPC) is gaining popularity for optimizing heat pump operations by considering future conditions and multiple control objectives [5]. In [6], an MPC approach is proposed to mitigate congestion events in the power grid by postponing the heating of water tanks and so minimizing peak loads. In [7], a hierarchical control framework is presented that evaluates the flexibility that a multienergy building system can offer in supporting power grid load shedding. In [8], an MPC is developed for the demand response of geothermal heat pumps aggregated in a virtual power plant. In [9], an economic MPC is developed to maximize the economic benefit of a multienergy hub. In [10], a multiagent approach using MPCs is presented to minimize the operation cost of a coupled heat and power grid via heat pumps.

However, most of these works do not consider heat pumps connected to a heating network. Heating grids are already widely used and low-temperature ones are expected to be

more and more used in the future to make use of waste heat sources. Since these solutions will often require busting heat pumps at the building level, it is important to consider this connection when assessing the power flexibility of heat pumps, as it affects the heat source temperature, which then influences their capacity and flexibility [11]. In [9] and [10], heat pumps connected to a heating network are considered, however, the work focuses mainly on economic benefits and does not fully evaluate the flexibility that heat pumps could provide to the power grid.

As presented in [12], coupled heat and power networks can be equipped with Integrated Energy Management Systems (IEMS), which provide scheduling and control functionalities based on Supervisory Control and Data Acquisition (SCADA) and state estimation. SCADA systems allow real-time data acquisition and processing, and the processed measurements are then used as inputs for the control. The control commands are subsequently sent to the controlled entities. It has to be noted that none of the works mentioned above considers the challenges associated with the practical implementation of the presented control solutions within a realistic environment. Only a few examples of realistic validations can be found. In [13], an MPC aimed at minimizing carbon emission of a multienergy building system is proposed and has been validated using an actual building setup. However, only a single building is considered, neglecting the rest of the heating network. In [14], a control architecture is presented to improve power grid resiliency under emergency conditions—using the flexibility provided by the multienergy buildings and is validated using a controller hardware-in-the-loop (CHIL) setup. However, no heat pump is considered and the control of the heating system is completely neglected.

In this article, we propose a centralized MPC that uses the operational flexible control of heat pumps so as to mitigate congestion in the power grid. The proposed approach extends the work presented in [15] by:

1) including transformers and cables capacity constraints in the MPC formulation;
2) including distributed energy resources (DER) scheduling in the MPC to assess the impact of DERs on the operation of the heating system, especially when considering the power constraints on the power grid;
3) including indoor temperature and heat demand flexibility by modeling the building as a lumped thermal zone.

Overall, the key contributions of this work are as follows:

1) development of an MPC formulation. We propose an MPC approach to manage heat pumps connected to a low-temperature district heating (LTDH) network while alleviating power grid congestion;
2) analysis of operational response. We examine how the heating system operates while adhering to power grid constraints, thus ensuring effective integration of heat pumps and functionality;

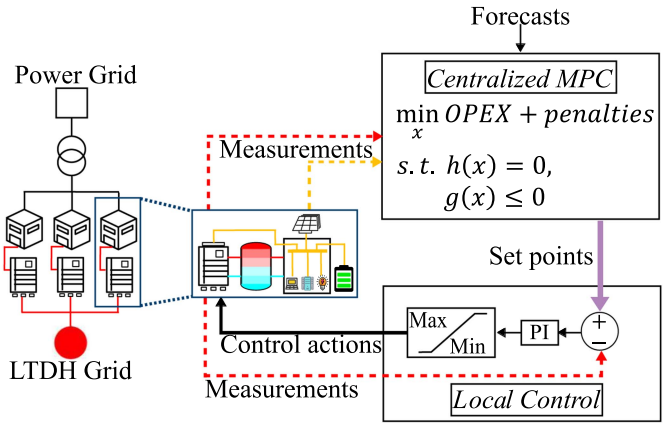

FIGURE 1. Schematic overview of the control architecture.

3) real-world implications study. We investigate the practical implications of implementing this control scheme, utilizing a Controller Hardware-in-the-Loop (CHIL) cosimulation setup for analysis.

The article is organized as follows: Section II introduces the hierarchical control structure proposed in this work. Section III provides an overview of the real-world system utilized in this study. Section IV details the approach and model development of the MPC. The implementation of direct control on heat pumps in the simulation model, along with its integration into the hardware-in-the-loop (HIL) cosimulation, is presented in Section V. Finally, the results and discussions are covered in Section VI and the work concludes in Section VII.

II. CONTROL ARCHITECTURE

Fig. 1 shows a schematic overview of the control architecture considered in this work. A centralized MPC is developed to control the Low-temperature District Heating (LTDH) network with heat pumps by minimizing its operational costs and penalties while considering constraints from both the LTDH network and the coupled power grid. Thus, the MPC includes constraints that prevent transformers and cables from being overloaded. Considered penalties are, for example, associated with thermal discomfort, thus arising from the difference between the actual indoor temperature and the desired one.

The dashed red and yellow lines in Fig. 1 indicate the communication flow of measurements to the centralized MPC from the LTDH network and the electrical systems, respectively. In addition to these measurements, the centralized MPC requires the forecasted values of the energy prices (gas and power) as inputs. All the inputs are sent to the MPC at regular intervals to trigger the MPC. A dedicated master script, developed in Python and introduced in [16], coordinates and synchronizes data transfer to the MPC. More information on the selected measurements and forecasted values are presented in Section V-B, while the detailed description of the MPC model can be found in Section IV. After receiving all inputs, the MPC performs the cost optimization and sends the

optimized set points to the local control of each heat pump, as underlined by the purple arrow in Fig. 1.

The block at the bottom of Fig. 1 provides a simplified overview of this local control, which includes Proportional-integral (PI) controllers aimed at directly changing the operational parameters of components, such as adjusting mass flow or temperature settings to follow the set points given by the MPC. The local control is developed to address the controllability of components in the studied real-world LTDH grid as well. It is worth noticing that the thermal measurements required for the feedback loop in the PI control differ from those provided to the MPC in both the specific parameters used and the time resolution. More information in this regard is detailed in Section V-A. Finally, the detailed design and implementation of the local control are discussed in Section V-A.

III. SYSTEM UNDER STUDY

The scenario considered in this work is inspired by the demo site constituted by the Living Lab Energy Campus (LLEC) [17], of Forschungszentrum Jülich (FZJ). Within this framework, focusing on the utilization of waste heat generated by the Jülich Supercomputing Center (JSC), seven buildings surrounding the JSC are being connected to a LTDH network. To supply heat, each building is equipped with a dedicated heat pump.

In addition, Distributed Energy Resources (DER) like Battery Energy Storage System (BESS) and photovoltaic (PV) systems are planned to be integrated into some of the seven considered buildings. Finally, a cloud-based Information and Communications Technology (ICT) platform is designed to monitor and control the integrated power and LTDH. In this context, the MPC algorithm presented in this article is envisioned to be integrated into the abovementioned ICT platform to control the components within the LTDH network, considering the constraints of both the LTDH grid and the power grid.

It is worth mentioning that the concepts presented in this article are not limited to the considered system, but can be easily extended to other frameworks where multienergy systems are considered, such as Energy Communities [18]. These are legal entities that empower citizens, small businesses, and local authorities to produce, manage, and consume their own energy. In such a context, the information gathered from the SCADA system can be integrated into a unique management platform, controlling both the electrical and the thermal domain.

A. COUPLING BETWEEN THE LTDH NETWORK AND THE POWER GRID

Fig. 2 shows the coupling of the power grid and the LTDH through heat pumps. In general, 10/0.4 kV transformers are used to supply multiple buildings, each one with a dedicated cable. From the 400 V busbar of the building, a dedicated cable is used to supply the heat pump, if present, and others for the "base load" and the DERs. The latter depends on the operations conducted daily in each building and is considered

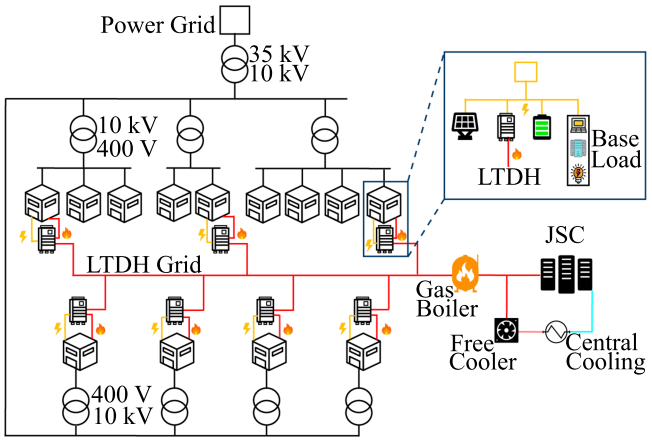

FIGURE 2. Schematic representation of the coupling between the power grid and the LTDH network.

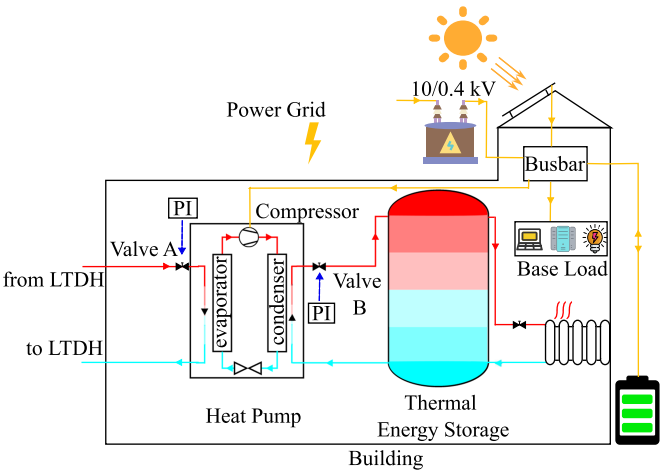

FIGURE 3. Energy supply of a building, heat, and power.

uncontrollable for the following analysis. A gas boiler is utilized to increase the supply temperature in the LTDH. The energy supply of each building includes the power supply and the thermal supply, which is illustrated in the right corner of Fig. 2. If there is excess waste heat from the supercomputers, a fan cooler free cooler (FC) and a water cooling system are used to cool the water flow.

B. ENERGY SUPPLY OF THE BUILDING

In Fig. 3, a detailed overview of a building's heat supply system and power supply system is shown. The diagram depicts the heat pump, the Thermal Energy Storage (TES), and the building system, with each component identified by the text below its illustration.

The building's heat supply is directly from TES, which is in turn supplied by the heat pump. The heat pump comprises three fluid circuits. The left circuit represents the water flow from and to the LTDH network. The central loop is the refrigerant loop, consisting of an evaporator, a compressor, a condenser, and an expansion valve. The right circuit,

connected to the TES, constitutes the heat supply to the user. In the heat exchange process, hot water from the LTDH grid heats the refrigerant in the evaporator. The warmed refrigerant is then compressed by the compressor and flows into the condenser, where it heats the cold water from the TES. In TES, heated water enters the tank from the top, while the cooled water is returned from the bottom. This results in a temperature gradient within the TES, where the upper layer has the highest temperature and it decreases moving toward the bottom. From the TES, the hot supply flow passes through a heater inside the building to warm up the air. The cooled water then returns to the TES from the bottom.

The blocks labeled with "PI" in Fig. 3 represent the PI controls which receive optimal set points from the MPC and adjust actuators to follow these set points. This is described in detail in Section V-A.

The power supply inside the building is depicted with the yellow color in Fig. 3. The heat pump, the base load, the rooftop PV panels, and the BESS are connected to the main busbar of the building. It is important to note that, within the LLEC project, not all buildings equipped with heat pumps will also have rooftop PV panels and dedicated BESS installed. However, in this study, to fully explore the impact of DER components, we assume that each building with a heat pump also has rooftop PV panels and a BESS.

C. SIMULATION OF THE LTDH NETWORK AND THE DISTRIBUTION GRID

The LTDH network and the distribution grid are simulated in two individual simulation models, as part of the Hardware-in-the-Loop (HIL) cosimulation setup to test the MPC. The heat supply system in each building and the LTDH network are simulated in Modelica using models from the AixLib library [19] and exported as a Functional Mock-up Unit (FMU). The simulation model of the LTDH network is extended from the works in [20], [21] by including local PI controls in each building. These controls are implemented to test the applicability of the proposed MPC on the physical system through a more realistic HIL framework.

Besides the seven buildings equipped with heat pumps, the whole distribution grid of the FZJ campus, including all voltage levels and components, is simulated in Simulink and run on the real-time simulator OPAL-RT. More information on this simulation model can be found in [16]. Due to the slow dynamic of the LTDH network, the model runs at a time step of 90 s, while the time step of the power system simulation in Simulink is 200 μs.

IV. MPC MODEL

An MPC utilizes mathematical model to predict and optimize future system behavior. In particular, it calculates control actions by solving an optimization problem that considers constraints and future predictions, based on the information from the controlled system at the current time (denoted as t). After the optimization, MPC provides a control action trajectory over a finite horizon (control horizon, denoted as N_c) $[\Delta u_t, \Delta u_{t+1}, \ldots, \Delta u_{t+N_c-1}]$. Following the receding horizon control principle, only the first control signal of the sequence is implemented in the controlled system. Then, the new measurements are used to calculate a new control trajectory. The prediction horizon (denoted as N_p) defines the number of time steps over which MPC makes predictions. That is, MPC predicts variables in the controlled system $[y_{t+1}, y_{t+2}, \ldots, y_{t+N_c-1}, \ldots y_{t+N_p}]$. It is noteworthy that the variables in the first $N_c - 1$ steps correspond to the control trajectory $[\Delta u_{t+1}, \ldots, \Delta u_{t+N_c-1}]$, excluding the control action at the current step t. To avoid confusion, the time interval within the control trajectory (thus, within the control horizon) is denoted as Δt_c, while the time interval within the prediction horizon is denoted as Δt_p [22].

A. ADAPTIVE PREDICTION HORIZON

In this work, the buildings with heat pumps are all office buildings and the heat pumps' supply is solely for space heating. The assumed working hours are from 08:00 to 19:00, a period with high base load and heat demand on the FZJ campus, increasing the possibility of grid congestion events. In addition, the base load during these hours tends to fluctuate more than during nontypical working hours due to various activities. Hence, a suitable time step duration Δt must be chosen in accordance with the reporting rate of the base load measurement (15 min). N_c is selected considering the dynamic response of the heat pump system. This is because N_c directly affects the increment of the control actions within the control trajectory that the MPC calculates to meet a specified control reference in the future [22]. Consequently, Δt_c and N_c are set to 15 min and 1 time step, respectively. The prediction horizon N_p is adjusted to balance the computational time required for real-time HIL cosimulation and to provide adequate advance notice for potential grid congestion. During nontypical working hours, with lower and less fluctuating base load and heat demand, a longer prediction horizon is advantageous for informing the TES about critical periods and allowing for recharging. Therefore, both a high prediction horizon and a long time interval are needed, in particular:

$$\begin{cases} N_p = 9,\ \Delta t_p = 15\ \text{min}, & \text{if } 06:00 \le t \le 19:00 \\ N_p = 13,\ \Delta t_p = 60\ \text{min}, & \text{otherwise} \end{cases} \tag{1}$$

Δt_p represents the time interval out of the control horizon N_c, where the interval within the control horizon is consistently set to 15 min. It is worth noting that the time interval begins to decrease from 06:00, two hours before the start of working hours, to provide more detailed information on power and heat demands, thereby enabling the necessary precharging of the TES for the peak period.

B. MATHEMATICAL MODELS IN THE MPC

The mathematical models used in the MPC for this study are adapted from those presented in [15], to align with the considered research framework. Thus, the original models are extended to consider the power supply modeling, for taking

into account the electrical constraints, DERs availability, to take into account power supply flexibility, and the building model, for thermal flexibility. In addition, the objective function is modified, to align with the purpose of flexibility assessment in the work. These modifications are addressed in subsequent sections, where the modeling of each component is described.

1) HEAT PUMP MODEL

With reference to the generic time step, $t = [1, 2, \ldots, N_p + 1]$ within the overall time horizon N_p+1, the heat exchange rate for both the evaporator and the condenser side, $Q_{evap,t}$ and $Q_{cond,t}$, can be determined as

$$Q_{evap,t} = m_{evap,t} \cdot c_p \cdot (T_{evap,in,t} - T_{evap,out,t}) \tag{2}$$

$$Q_{cond,t} = m_{cond,t} \cdot c_p \cdot (T_{cond,out,t} - T_{cond,in,t}) \tag{3}$$

where $m_{evap,t}$ and $m_{cond,t}$ are the mass flows. $T_{evap,in,t}$ and $T_{cond,in,t}$ are the water temperatures of the LTDH network and the TES circuit into the heat exchangers which exchange heat with the refrigerants in heat pumps, while $T_{evap,out,t}$ and $T_{cond,out,t}$ are the water temperatures out of the heat exchangers. c_p is the heat capacity of water.

The relation between the power consumption $P_{el,t}$ and the heat flow rates is formulated as

$$Q_{cond,t} = Q_{evap,t} + P_{el,t} \tag{4}$$

with the Coefficient of Performance (COP), defined as

$$COP = \frac{Q_{cond,t}}{P_{el,t}} \tag{5}$$

COP is also a function of the refrigerant temperature that flows out of the condenser (denoted as $T^*_{cond,out,t}$) and that out of the evaporator (denoted as $T^*_{evap,out,t}$):

$$COP = \frac{T^*_{cond,out,t}}{T^*_{cond,out,t} - T^*_{evap,out,t}} \cdot \eta_{pl} \cdot \eta_{carnot} \tag{6}$$

where η_{pl} and η_{carnot} are part-load and Carnot efficiency. According to the manufacturer data sheet [23], the COP is constrained to be less than 5.5 for heat pumps. In the heat pump model presented in [15], when modeling the COP, $T^*_{cond,out,t}$ is assumed to be equal to $T_{cond,out,t}$ and $T^*_{evap,out,t}$ is equal to $T_{evap,out,t}$. In this study, since the electrical constraints are considered in the MPC to control heat pumps' power consumption, a more accurate modeling of the heat pump's power consumption within the MPC is needed. Thus, to align the optimal power consumption reference provided by the MPC with the heat pump's power consumption in the simulation model, the differences in these temperatures are considered.

In the simulation model, $T^*_{cond,out,t}$ and $T^*_{evap,out,t}$ have a nonlinear relationship with $T_{cond,out,t}$ and $T_{evap,out,t}$, respectively. As a simplification, since the heat absorption and release processes in the refrigerant are not crucial for the control decisions, in the MPC $T^*_{cond,out,t}$ and $T^*_{evap,out,t}$ are assumed to have a fixed ratio to the corresponding water temperatures in the TES circuit and in the LTDH network:

$$T^*_{cond,out,t} = T_{cond,out,t} \cdot \alpha_{cond} \tag{7}$$

$$T^*_{evap,out,t} = T_{evap,out,t} \cdot \alpha_{evap} \tag{8}$$

where α_{cond} and α_{evap} are constants. In general, since the condenser outlet temperature of the refrigerant $T^*_{cond,out,t}$ is consistently higher than the condenser outlet temperature of the water $T_{cond,out,t}$, α_{cond} is greater than 1. Then, since the evaporator outlet temperature of the refrigerant $T^*_{evap,out,t}$ is lower than the evaporator outlet temperature of the water $T_{evap,out,t}$, α_{evap} is expected to be lower than 1. In this work, to align the MPC model with the simulation model, and to reflect the physical phenomena observed in the system, the coefficients α_{cond} and α_{evap} have been calibrated to 1.005 and 0.992, respectively. In particular, such values have been tuned by comparing the simulation results, here considered as the reference, with the optimization results from the MPC.

2) TES MODEL

The State of Charge (SOC) of the TES is modeled as a state variable:

$$SOC_{TES,t} = SOC_{TES,t-1} + \frac{(Q_{cond,t} - Q_{supply,t}) \cdot \Delta t}{E_{TES,cap}} \tag{9}$$

where $Q_{supply,t}$ is the heat flow supplied to the end user from the TES, $E_{TES,cap}$ is the overall capacity of the TES, and Δt represents the time interval, which can be either the control interval Δt_c or the prediction interval Δt_p. In the considered scenario, the TES is filled with water. The TES is built with structural steel and insulated with a polyester fiber fleece in a durable polystyrene shell, which has a thermal resistance of approximately $0.36\,W/m^2\,K^{-1}$. The TES units are located indoors. Given the dimensions of the TES and an average temperature difference between inside and outside of 40 °C, the heat loss is 0.1 kW. Consequently, with an energy capacity of around 100 kWh, the heat loss has a negligible impact on the control's accuracy. Therefore, to simplify the model, it is reasonable to consider the TES as perfectly insulated, as in [15]. The volume of the TES is set to 2 m^3 for all buildings. The value is in line with the TES installed on the FZJ campus. The energy capacity of TES depends on the parameters of the TES [15]:

$$E_{TES,cap} = V_{TES} \cdot \rho \cdot c_p \cdot (T_{TES,top} - T_{TES,bottom}) \tag{10}$$

where V_{TES} is the volume of the TES, ρ and c_p are the water density and specific heat capacity of water, respectively. $T_{TES,top}$ and $T_{TES,bottom}$ are the temperature at the top and the bottom layers of the TES. The assumption in [15] is also used in this work:

$$T_{TES,top} = T_{c,in} \tag{11}$$

$$T_{TES,bottom} = T_{c,out} \tag{12}$$

where $T_{c,in}$ and $T_{c,out}$ are the water supply temperature and return temperature of the buildings, respectively. These two

TABLE 1 Parameters for All Building Models

Building name	$U_w A_w$ [kW/K]	$U_r A_r$ [kW/K]	$U_o A_o$ [kW/K]	$U_g A_g$ [kW/K]	V_{air} [m^3]
A	2.87	4.61	3.02	4.81	8304.57
B	1.68	2.58	1.62	2.69	10384.62
C	3.63	1.95	4.16	2.19	9621.05
D	1.25	0.76	0.83	0.93	10059.24
E	0.11	0.046	0.096	0.056	858.88
F	0.094	0.11	0.094	0.13	2151.26
G	0.45	0.51	0.45	0.83	4221.02

values are parameters for the MPC and are determined as a linear function of the ambient temperature. Therefore, the TES in this work is not assumed as well mixed.

Furthermore, to discourage small and continuous charging/discharging behavior, which has a minor impact on the operational costs but can lead to inefficiency, a cost penalty has been introduced:

$$\lambda_{TES} = w_{TES,t} \cdot (Q_{cond,t} - Q_{supply,t})^2 \tag{13}$$

λ_{TES} is the penalty and w_{TES} is its weight in the multiobjective function. The penalty is based on the squared change in TES energy. The weight w_{TES} is set at 0.01 € /kW^2, allowing an optimal precharge of the TES for providing flexibility when the heat pump power supply is limited, while preventing small continuous charging/discharging inefficient behavior of the TES.

3) BUILDING MODELS

In this section, the building models used in the considered case studies are described. While these models are tailored to our analysis, the mathematical equations can be easily adapted for other contexts, with specific parameters.

Each building is assumed as one lumped thermal zone. The considered heat loss of each building is

$$Q_{loss,t} = \sum_{\varepsilon \in envelope} U_\varepsilon \cdot A_\varepsilon \cdot (T_{room,t} - T_{amb,t}) + U_{ground} \cdot A_{ground} \cdot (T_{room,t} - T_{ground,t}). \tag{14}$$

The term "envelope" refers to a building's windows, outer walls, and roofs. The overall heat transfer coefficient, namely U_ε, is the heat rate transferred per unit area per unit temperature difference between two objects. For simplicity, in Table 1, the values for the product of the overall heat coefficient and the area are given, which are derived using the Python toolbox Teaser [24]. The subscripts $_w$, $_r$, $_o$, and $_g$ indicate the windows, roof, outer walls, and ground, respectively. It is worth noting that the values of the product for buildings can vary significantly, as the areas of different buildings can differ substantially. In addition, also the air volume V_{air} is calculated based on the number of floors and the net floor area of buildings utilizing the Teaser toolbox. The buildings' parameters of the seven considered buildings are shown in Table 1. Out of the considered seven buildings, three (in the following labeled as A, B, and C) are particularly relevant due to their grid congestion issues. $T_{room,t}$, $T_{amb,t}$, and $T_{ground,t}$ are the air temperature in the building, ambient temperature, and the ground temperature, respectively. The historical weather data are used as perfect foresight values for ambient temperature, while the ground temperature is considered constant at 8 °C [25].

The temperature variation in the building is subjected to

$$c_{p,air} \cdot \rho_{air} \cdot V_{air} \cdot \frac{T_{room,t} - T_{room,t-1}}{\Delta t} = Q_{demand,t} - Q_{loss,t} \tag{15}$$

where $c_{p,air}$ is the air heat capacity at standard conditions, with ρ_{air} and V_{air} representing the air density and volume inside the building, respectively. The required heat demand $Q_{demand,t}$ to keep the building at a certain temperature is supplied from the TES ($Q_{supply,t}$). $T_{room,t}$ is constrained as

$$T_{room,set,t} - \Delta T_{room,set,t} \le T_{room,t} \le T_{room,set,t} + \Delta T_{room,set,t} \tag{16}$$

where $T_{room,set,t}$ is the design indoor temperature in the building, which is set as

$$T_{room,set,t} = \begin{cases} 22\,°C, & \text{if } 08:00 \le t < 19:00 \\ 18\,°C, & \text{otherwise} \end{cases} \tag{17}$$

and $\Delta T_{room,set,t}$ is the maximal deviation of $T_{room,t}$. The penalty $\lambda_{thermal\ discomfort}$, formulated as "cost" for thermal discomfort, is calculated based on the squared difference between $T_{room,set,t}$ and $T_{room,t}$:

$$\lambda_{thermal\ discomfort} = w_{thermal\ discomfort} \cdot (T_{room,set,t} - T_{room,t})^2. \tag{18}$$

The penalty weight $w_{thermal\ discomfort}$ must be carefully selected to provide thermal flexibility by adjusting the indoor temperature during congestion periods while avoiding temperature reductions only for saving energy costs when there is no congestion. This parameter is set at 3, which after numerous tests has been determined to be the optimal compromise between the two factors mentioned above.

4) POWER SUPPLY–BASE LOAD

The total apparent power of the loads on the ith building $S_{L,i,t}$, includes based load $S_{base\ load,i,t}$, and heat pump consumption $S_{hp,i,t}$, if present. The building is then supplied with one cable from the medium voltage/low voltage transformer substation, which has an ampacity $I_{cable,max,i}$. Each transformer j with rated power $S_{trafo,\ nom,\ j}$, supplies more than one building. Consequently, for each building, the apparent power balances can be written as

$$S_{L,i,t} + S_{Gen,i,t} = S_{cable,i,t} \tag{19}$$

where $S_{cable,i,t}$ is the apparent power flowing through the cable to the building i. $S_{Gen,i,t}$ represents the power generation in building i, which includes the generation from DER, as introduced in detail in the next section. For each transformer, the apparent power balance is

$$S_{L,\ j,t} + S_{Gen,\ j,t} = S_{trafo,\ j,t} \tag{20}$$

where $S_{\mathrm{L},j,t}$ denotes the total load of the transformer j, which includes the heat pump loads and base loads from all of the buildings supplied by transformer j. $S_{\mathrm{Gen},j,t}$ denotes the total apparent power supplied to transformer j by the PVs and BESSs. $S_{\mathrm{trafo},j,t}$ is the apparent power flowing through transformer j.

Then, the cable and the transformer constraints are implemented as

$$\frac{S_{\mathrm{cable},i,t}}{V_{\mathrm{nominal},i}} \leq I_{\mathrm{cable,max},i} \tag{21}$$

$$S_{\mathrm{trafo},j,t} \leq S_{\mathrm{trafo,nom},j} \tag{22}$$

where $V_{\mathrm{nominal},i}$ is the nominal voltage of the busbar where the building i is connected. It has to be noted that, given the ampacity of the cable, it is necessary to convert the apparent power flowing through the cable $S_{\mathrm{cable},i,t}$, into an equivalent current value. This conversion is achieved by dividing the apparent power $S_{\mathrm{cable},i,t}$ by the nominal voltage $V_{\mathrm{nominal},i}$.

5) DER–PV AND BESS SYSTEM

The generic PV system installed in building i can be modeled as

$$P_{\mathrm{pv},i,t} \leq P_{\mathrm{pv,max},i} \tag{23}$$

where $P_{\mathrm{pv},i,t}$ and $P_{\mathrm{pv,max},i}$ are the actual generated active power and maximum active power that can be generated by the PV system, respectively. In particular, $P_{\mathrm{pv,max},i}$ is estimated from the number of PV modules assumed on the rooftop and the forecasted Global Horizontal Irradiance (GHI). In particular, the latter is assumed as perfect foresight and utilizes historical weather data. The power factor is assumed to be 1.

The SOC of the BESS of the ith building is modeled as

$$SOC_{\mathrm{BESS},i,t+1} = SOC_{\mathrm{BESS},i,t} + \left(\eta_{\mathrm{c},i,t} \cdot P_{\mathrm{c},i,t} - \frac{P_{\mathrm{dis},i,t}}{\eta_{\mathrm{dis},i,t}}\right) \cdot \frac{\Delta t}{E_{\mathrm{BESS},i}} \tag{24}$$

where

$$0 \leq P_{\mathrm{c},i,t} \leq P_{\mathrm{c,max},i} \cdot u_{\mathrm{battery},i,t} \tag{25}$$

$$0 \leq P_{\mathrm{dis},i,t} \leq P_{\mathrm{dis,max},i} \cdot (1 - u_{\mathrm{battery},i,t}) \tag{26}$$

$$\mathrm{SOC_{BESS,min}} \leq \mathrm{SOC_{BESS},}_{i,t} \leq \mathrm{SOC_{BESS,max}} \tag{27}$$

where $P_{\mathrm{c},i,t}$ and $P_{\mathrm{dis},i,t}$ are the charging and discharging rate of battery, while $\eta_{\mathrm{c},i,t}$ and $\eta_{\mathrm{dis},i,t}$ are the charging and discharging efficiency of battery, which are assumed to be 0.9 for all buildings. $SOC_{\mathrm{BESS,min}}$ and $SOC_{\mathrm{BESS,max}}$ are the minimal and maximal SOC level, which are assumed to be 30% and 90%, respectively. The power factor of battery's converter is assumed to be 1. $u_{\mathrm{battery},i,t}$ is the binary variable to indicate the operational state of the battery, where 1 indicates that the battery charges. $E_{\mathrm{BESS},i}$ is the battery capacity installed in the building i. In Table 2, the parameters of PVs and BESSs are given for each building. It is worth noting that the maximal active power of the PV for each building is determined based on the assumed total number of PV panels installed on the roof of the same building. This number depends on the actual area of the building's roof foreseen for the installation. Starting from these values, in line with the specifications of the systems already installed on the FZJ campus and the average base load of each building, the BESS capacity has been chosen for each building, as well as their discharging and charging power rates.

TABLE 2 Nominal Parameters of PV and BESS System

Building Unit	$P_{\mathrm{pv,max}}$ [kWp]	E_{BESS} [kWh]	$P_{\mathrm{dis,max}}$ [kW]	$P_{\mathrm{c,max}}$ [kW]
A	100	100	40	40
B	150	150	40	40
C	60	60	40	40
D	100	100	40	40
E	10	10	20	20
F	15	15	20	20
G	80	80	40	40

The $S_{\mathrm{L},i,t}$ and $S_{\mathrm{Gen},i,t}$ of the building i are formulated as follows, considering the PV generation and the charging of the BESS:

$$S_{\mathrm{L},i,t} = S_{\mathrm{hp},i,t} + S_{\mathrm{base\ load},i,t} + S_{\mathrm{c},i,t} \tag{28}$$

$$S_{\mathrm{Gen},i,t} = S_{\mathrm{pv},i,t} + S_{\mathrm{dis},i,t} \tag{29}$$

where $S_{\mathrm{pv},i,t}$ is the apparent power of the PV inverter, $S_{\mathrm{dis},i,t}$ and $S_{\mathrm{c},i,t}$ are discharging and charging apparent power of the BESS inverter, respectively. The aforementioned equations can be applied to $S_{\mathrm{L},j,t}$ and $S_{\mathrm{Gen},j,t}$ as well.

6) OBJECTIVE FUNCTION

The objective function of the MPC is defined as

$$\sum_{t \in N_{\mathrm{p}}+1} \Bigg(E_{\mathrm{gas\ boiler},t} \cdot \xi_{\mathrm{natural\ gas}} + E_{\mathrm{CC},t} \cdot \xi_{\mathrm{CC}} + \left[E_{\mathrm{FC},t} + E_{\mathrm{pump},t} + \sum_{i \in C} E_{\mathrm{HP},i,t} \right] \cdot \xi_{\mathrm{el}} + \sum_{i \in C} \left(\lambda_{\mathrm{TES},i,t} + \lambda_{\mathrm{thermal\ discomfort},i,t} \right) \Bigg) \tag{30}$$

where the first three terms are operational costs. $E_{\mathrm{gas\ boiler},t}$ and $E_{\mathrm{CC},t}$ are the energy consumed by the gas boiler and central cooling (CC), while $\xi_{\mathrm{natural\ gas}}$ and ξ_{CC} are the corresponding prices. The electricity cost considers the electricity consumed by the FC $E_{\mathrm{FC},t}$ the LTDH network pump $E_{\mathrm{pump},t}$, and each heat pump $E_{\mathrm{HP},i,t}$. C represents the set of buildings. In addition to the operational costs included in the objective function of the original model [15], penalties for using the TES, $\lambda_{\mathrm{TES},i,t}$, and for thermal discomfort, $\lambda_{\mathrm{thermal\ discomfort},i,t}$, introduced in Sections IV-B-2 and IV-B-3, respectively, are also included. It is worth noting that an economic MPC using purely economic cost functions will not fit well with this application due to the penalty term associated with thermal

discomfort. We analyze the effect of this term in a dedicated case study in Section VI-D.

7) OVERALL MPC FORMULATION

This section summarizes the overall MPC formulation, while the previous sections describe individual components. Considering the generic time step, $t = [1, 2, \ldots, N_p + 1]$ within the overall time horizon N_p+1, the objective function and the constraints of the MPC can be summarized as

$$\begin{aligned}\min \sum_{t \in N_p+1} \Bigg(& E_{\text{gas boiler},t} \cdot \xi_{\text{natural gas}} + E_{\text{CC},t} \cdot \xi_{\text{CC}} \\ & + \left[E_{\text{FC},t} + E_{\text{pump},t} + \sum_{i \in C} E_{\text{HP},i,t} \right] \cdot \xi_{\text{el}} \\ & + \sum_{i \in C} \left(\lambda_{\text{TES},i,t} + \lambda_{\text{thermal discomfort},i,t} \right) \Bigg) \end{aligned} \tag{31}$$

s.t.

heat pump constraints	(2)–(4), (6), (7)–(8) $\forall C$
TES constraints	(9)–(12) $\forall C$
building constraints	(14)–(16) $\forall C$
power supply constraints	(19)–(22), (28)–(29) $\forall C$
DER constraints	(23)–(27) $\forall C$
$LTDH$ network constraints	as in [15].

In the formulation, the objective function presented in (30) is minimized. The term $E_{\text{gas boiler},t}$ represents the total energy consumption by the gas boiler, with $\xi_{\text{natural gas}}$ denoting the gas price. Similarly, $E_{\text{CC},t}$ is the energy consumption by the CC, and ξ_{CC} is the corresponding price. $E_{\text{FC},t}$, $E_{\text{pump},t}$, and $E_{\text{HP},i,t}$ are the electricity consumption by the FC, the LTDH network pump and the heat pumps, respectively, with ξ_{el} denoting the electricity price. The index set C comprises all the buildings considered in this work, namely buildings A through G. In addition, $\lambda_{\text{TES},i,t}$ and $\lambda_{\text{thermal discomfort},i,t}$ are penalty items for the TES and the thermal discomfort, reflecting the deviation between the design indoor temperature and the actual indoor temperature. The optimization of the objective function is subject to these constraints: the constraints related to the heat pumps (introduced in Section IV-B-1), the TES units (Section IV-B-2), the building models (Section IV-B-3), the power supplies (Section IV-B-4), and the DERs (Section IV-B-5). It is worth noting that the constraints for the LTDH network have been already presented in [15] and, for simplicity, these are not reported again in this work.

V. HIL VALIDATION

The proposed MPC is tested and validated in a HIL framework. This framework is composed of a cosimulation setup and a cloud-based controller, with the latter serving as the device under test. Detailed descriptions of each component within this framework can be found in Section V-B.

A. LOCAL CONTROL OF HEAT PUMPS

The local control of each heat pump implements the optimal set points from the MPC in the simulation model of the LTDH network. The simulation model of the LTDH network is detailed in [20] and [21]. Based on the actuators' accessibility to the customers, as detailed in the manufacturer data sheet [23], $T_{\text{evap,out}}$, $T_{\text{cond,out}}$, and SOC_{TES} in each heat pump are chosen as set points. $T_{\text{cond,out}}$ can be set directly, while $T_{\text{evap,out}}$ and SOC_{TES} are implemented through PI controls. In addition to the local control set points for each heat pump, the supply temperature in the LTDH network $T_{\text{net,in}}$, and the return water temperature from the user side $T_{\text{user,out}}$, are also selected as set points transferred from the MPC to the simulation model. These are transferred from the MPC to the simulation model.

In the following, the PI controls are detailed, starting from the description of the design and the implementation of the SOC_{TES} control. Based on the scheme presented in Fig. 3, where the condenser side is depicted on the left side of the TES and the user side is represented on the right side of the TES, the variation of SOC_{TES} is modeled as

$$\Delta SOC_{\text{TES}} = \frac{(Q_{\text{cond}} - Q_{\text{user}}) \cdot \Delta t}{E_{\text{TES,cap}}} \tag{32}$$

where Q_{user} and Q_{cond} are expanded as

$$Q_{\text{cond}} = m_{\text{cond}} \cdot c_p \cdot \Delta T_{\text{cond}} \tag{33}$$

$$Q_{\text{user}} = m_{\text{user}} \cdot c_p \cdot \Delta T_{\text{user}} \tag{34}$$

ΔT_{cond} and ΔT_{user} represent the differences in the condenser and user side temperatures, respectively. Specifically, $\Delta T_{\text{cond}} = T_{\text{cond,out}} - T_{\text{cond,in}}$ and $\Delta T_{\text{user}} = T_{\text{user,in}} - T_{\text{user,out}}$.

In Fig. 3, $T_{\text{cond,out}}$ and $T_{\text{user,in}}$, as well as $T_{\text{cond,in}}$ and $T_{\text{user,out}}$, are at the same levels in the TES and can thus be considered equal. Therefore, ΔT_{cond} and ΔT_{user} are also assumed to be the same. Thus, (32) can be reformulated as

$$\Delta m_{\text{TES}} = \frac{V_{\text{TES}} \cdot \rho_{\text{water}}}{\Delta t} \cdot \Delta SoC_{\text{TES}} \tag{35}$$

where $\Delta m_{\text{TES}} = m_{\text{cond}} - m_{\text{user}}$ is the net mass flow that flows into the TES, and V_{TES} is the volume of the TES. Therefore, the SOC_{TES} is controlled by controlling the net mass flow into the TES. Since the m_{user} is determined on the user side, Δm_{TES} is controlled by the condenser's mass flow. Rewriting (35) into a form that uses a multiplier for the proportional part and an integrator for the integral part, (36) can be obtained

$$\Delta m_{\text{TES}} = K_p \cdot \Delta SOC_{\text{TES}} + \frac{K_p}{T_i} \int \Delta SOC_{\text{TES}}\, dt \tag{36}$$

where K_p and T_i are the proportional gain and the time constant of the integral part of the PI control and are set to 2.217 and 500, respectively. These values are tuned to maintain the system's overshoot within 10% and a small settle time within the control interval. The implementation of this PI control is illustrated in Fig. 4, and it corresponds to the control of valve B in Fig. 3.

The deviation between the reference $SOC_{\text{TES,ref}}$ and the actual measurement is processed by the PI controller, producing

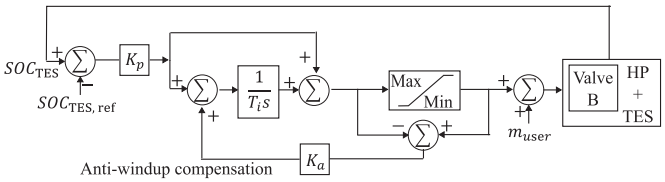

FIGURE 4. Implementation of SOC_{TES} PI control.

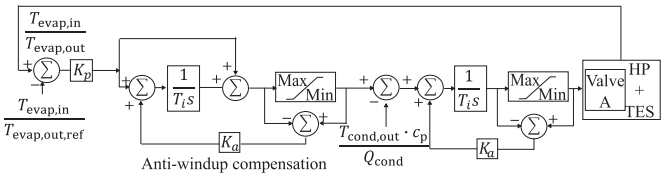

FIGURE 5. Implementation of $T_{evap,out}$ PI control.

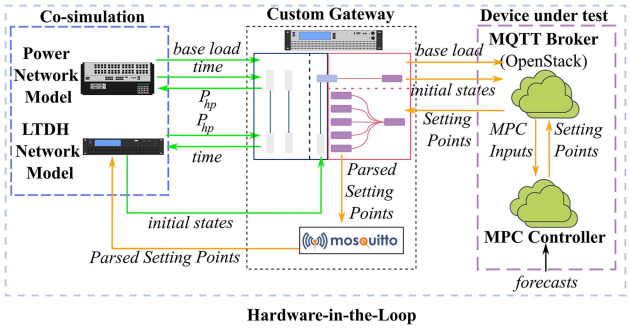

FIGURE 6. HIL cosimulation platform and communication interfaces.

an adjustment in the net mass flow into the TES. To determine the total mass flow through the condenser, this adjusted value is added with m_{user}, as shown in Fig. 4. Subsequently, the valve position within the condenser loop is modified to match this flow requirement. This valve is illustrated in Fig. 3 and named valve B. Meanwhile, the SOC_{TES} is measured and fed back into the PI control.

The PI control of the $T_{evap,out}$ is implemented as follows. Formulating P_{el} as a function of Q_{cond} and COP, from (5) into (4), the following equation is obtained:

$$Q_{evap} = Q_{cond}\left(1 - \frac{1}{COP}\right). \tag{37}$$

The modeling of COP in (6) is approximated using the ideal Carnot efficiency $\frac{T_{cond,out}}{T_{cond,out}-T_{evap,out}}$, and Q_{evap} is expanded as (2), the relation between the evaporator's mass flow and its return temperature is obtained:

$$m_{evap} = \frac{Q_{cond}}{T_{cond,out} \cdot c_p \cdot \left(\frac{T_{evap,in}}{T_{evap,out}} - 1\right)}. \tag{38}$$

$T_{cond,out}$, $T_{evap,in}$, and Q_{cond} are independent of the evaporator mass flow and the return temperature. $T_{cond,out}$ is the set point, $T_{evap,in}$ is determined by the set point of supply temperature $T_{net,in}$ in the LTDH network. Q_{cond} is a function of $T_{cond,out}$, $T_{cond,in}$ and m_{cond}. $T_{cond,in}$ and m_{cond} are determined by the set point $T_{user,out}$ and the TES PI control, respectively. Reformulating (38), the relation between the variation of the evaporator's mass flow and the variation of the return flow temperature is obtained:

$$\Delta\left(\frac{1}{m_{evap}}\right) = \frac{T_{cond,out} \cdot c_p}{Q_{cond}}\left[\Delta\left(\frac{T_{evap,in}}{T_{evap,out}}\right) - 1\right] \tag{39}$$

where

$$\Delta\left(\frac{T_{evap,in}}{T_{evap,out}}\right) = \left(\frac{T_{evap,in,t}}{T_{evap,out,t}}\right) - \left(\frac{T_{evap,in,t-1}}{T_{evap,out,t-1}}\right).$$

By reformulating (39) into the form presented in (36), the following equation is obtained:

$$\Delta\left(\frac{1}{m_{evap}}\right) = K_p \cdot \Delta\left(\frac{T_{evap,in}}{T_{evap,out}}\right) + \left(\frac{K_p}{T_i}\right)\int \Delta\left(\frac{T_{evap,in}}{T_{evap,out}}\right) dt - \frac{T_{cond,out} \cdot c_p}{Q_{cond}} \tag{40}$$

K_p and T_i are set to 3.5 and 100, respectively, and are tuned to ensure a good control performance as discussed in the SOC_{TES} control. The corresponding PI control is shown in Fig. 5. Such control is applied to valve A of Fig. 3, to regulate the evaporator mass flow.

The PI control receives deviations between the ratios of $\frac{T_{evap,in}}{T_{evap,out}}$ and $\frac{T_{evap,in}}{T_{evap,out,ref}}$. Its output, added to $-\frac{T_{cond,out} \cdot c_p}{Q_{cond}}$, determines the reciprocal of the evaporator mass flow increment $\frac{1}{m_{evap}}$ in (39). This reciprocal is then added to the previous time step's evaporator mass flow reciprocal to calculate the current evaporator mass flow. The valve position is adjusted and the measurement feedback is provided to the PI control. The antiwindup compensation has been implemented and K_a is set to 1.1 in both PI controllers.

B. INTEGRATION INTO THE HIL COSIMULATION PLATFORM

In Fig. 6, the HIL cosimulation platform is shown. The platform consists of the cosimulation (within the blue dotted block) and the control under test (within the purple dotted block).

The cosimulation includes the power grid model, running on the real-time simulator OPAL-RT 5033XG with 8 Intel Xeon cores, 3.8 GHz, with a time step of 200 µs, and the LTDH simulation model, exported as FMU and running on a PC with CPU 2.99 GHz, 64 GB RAM, at a time step of 90 s, due to the slower dynamics. The green lines represent data communication using User Datagram Protocol (UDP), while the orange ones represent Message Queues Telemetry Transport (MQTT). UDP protocol is chosen as a tradeoff between message size, transmission speed, and setup complexity. At the beginning of a communication round, the power grid model shares its simulation time with the LTDH model for synchronization, which then sends back the heat pump's power consumption data.

Within the HIL interface, the device under test communicates with the cosimulation using a MQTT broker on the cloud. The control interval of MPC is 15 min to match the heat pumps' slow dynamic response. The MPC runs on an OpenStack platform with 32 GB RAM, using the GUROBI 10.0.3 solver [26], allowing nonconvex quadratic constraints. The optimality gap threshold is set to 5%, and the maximal solution time is set to 60 s to meet the requirement of the real-time implementation. At each HIL communication interval, a Python script on the PC collects initial states from the FMU and forecasts data like energy prices, ambient temperature, base load, and heat demand, and forwards them to the MPC. The data are sent to MPC every 15 min. It is worth noting that, in order to purely evaluate the efficacy of the control framework without the influence of external factors, such as the forecast accuracy, the averages of the energy prices of the year considered in this test (i.e., 2019) are considered as input for the forecasted energy prices. However, the proposed control framework can already include variable forecasts of energy prices. Meanwhile, the power grid model updates the control with its base load. The base load is used to calculate the available capacity for heat pumps, considering as the uncontrollable loads. The MPC optimization uses real-time data for its first step and forecasts for the rest. After optimizing, it sends the optimal set points back through the MQTT broker, and the LTDH model adjusts its low controls and starts new simulations based on these set points.

In the setup, OPAL-RT's simulation time is the standard time for all components [16]. During each cosimulation interval, OPAL-RT shares its time with the PC cluster running the LTDH model, which then adjusts its time accordingly. Both the power grid model and the LTDH model use their local times to send data to the MPC controller.

A dedicated node-red-based open-source communication gateway, labeled as "Custom Gateway" in Fig. 6, serves as a central communication interface. This gateway also includes an algorithm that automatically maps the MPC's set points into simulation model parameters, more information in this regard can be found in [27].

VI. RESULTS AND ANALYSIS

In this section, five case studies are considered and the outcomes are discussed. Starting from a base case, namely Case 0—where the MPC, based on the approach described in [15], takes into consideration only the thermal constraints—the impact of the power constraints, DER, and flexible indoor temperature are evaluated with an incremental approach. In Case 1, the impact of power constraints is evaluated with respect to Case 0. Starting from the base case, the transformer capacity and the cable capacity constraints described in (21) and (22) are included in the MPC formulation, while PV generation and BESS usage are not included and the indoor temperatures are maintained constant. Thus, by exploring the effects of power constraints on the MPC, with case study 1 we analyze how the district heating network and TES operation are affected by the power grid constraints. Once the impact of the power constraints has been evaluated, Case 1 becomes the benchmark case for all the following analyses. In Case 2, the impact of DER is evaluated. Thus, while considering the power constraints in the MPC and the fixed indoor temperature, each building is equipped with rooftop PV panels and a BESS. This case study focuses on exploring how the integration of DERs influences the operation of the TES and LTDH network when power constraints are considered. In Case 3, the impact of indoor temperature is evaluated. To do so, the power constraints are still included in the MPC while the DERs are neglected. To investigate the impact of adjustable indoor temperature settings on the operation of TES and LTDH network, and meet the power constraints, the maximal allowable deviation in indoor temperature $\Delta T_{\text{room,set}}$ is set to 2 °C in the constraint defined by (16). For the comparison, $\Delta T_{\text{room,set}}$ in Case 1 is set to 0 °C. Finally, Case 4 combines Case 2 and Case 3. Each building is equipped with rooftop PV panels and a BESS, while the maximal allowable deviation in indoor temperature $\Delta T_{\text{room,set}}$, is set to 2 °C. This case study explores how these components can be coordinated to provide the required power flexibility. Table 3 summarizes the considered cases.

All use cases use data from a typical winter day in 2019. Specifically, the ambient temperature as well as the GHI measurements at FZJ are used to calculate the heat demand for space heating in buildings and the maximal available PV generation. In this work, the BESS is assumed to be charged from the previous day with an initial SOC of 0.9 and the SOC of TES is set to 0.4, to demonstrate the precharging effect due to the advance notification of congestion events by the MPC.

An online MPC implementation must meet real-time constraints, which is particularly challenging for the proposed MPC due to its nonconvex and nonlinear nature, requiring significant computational power [28], [29]. Therefore, a strategy is adopted, where feasibility is prioritized over optimality [30]. This allows the MPC to update control decisions in a timely manner. In this work, the maximal allowable resolution time for the MPC is set to 60 s. The average optimality gap at the maximal resolution time limit is 45%, for the cases where the power constraints are included. For the case without the power constraints, the average optimality gap is 31%. Thus, some optimality is sacrificed to ensure timely updates from the MPC. Several factors would increase the computational burden of the MPC, including its formulation, the power constraints, and the length of the time horizon. Specifically, the nonlinear and nonconvex formulation in the MPC, the inclusion of power constraints, and a longer time horizon add computational complexity and thus increase the resolution time for the MPC to find the optimal solution.

A. CASE STUDY 0—BASE OPERATION OF THE HEAT PUMPS

With Case 0, the base operation of the heat pumps is analyzed. The MPC minimizes the operation cost without taking into consideration the power constraints, neglecting the DER and assuming the indoor temperature set-point constant. The

TABLE 3 Overview of the Considered Cases

Case study	Components	Indoor temperature	Power constraints	Objective to be evaluated	Benchmark Case
Case 0	LTDH, TES, heat pump	fixed	no	Base operation of the heat pumps	none
Case 1	LTDH, TES, heat pump	fixed	yes	Impact of power constraints	Case 0
Case 2	LTDH, TES, heat pump, PV, BESS	fixed	yes	Impact of DER (i.e., PV and BESS)	Case 1
Case 3	LTDH, TES, heat pump	flexible	yes	Impact of flexible indoor temperature	Case 1
Case 4	LTDH, TES, heat pump, PV, BESS	flexible	yes	Impact of DER and flexible indoor temperature	Case 1

results are summarized in Fig. 7, where the blue curves show a one-day profile of operation on building C.

Fig. 7(a) and (b) shows the apparent power supplied from the transformer and current through the cable, respectively. The base load is shown in green. Since no power constraints are included, the blue curves sometimes exceed the maximal capacity of the transformer or the ampacity of the cable, which are indicated as red dashed lines in the two subplots. Similarly, in Fig. 7(c), where the active power consumption of the heat pump is shown, the blue curve exceeds the maximal allowed active power consumption by the heat pump (red dashed line), which is derived from the transformer and cable capacities as for (21) and (22). The congestion starts at 08:00 and ends at 19:00, which is consistent with the time period defined in (17) when the desired indoor temperature is increased. Fig. 7(d) shows the heat output of the heat pump. A peak is observed at 08:00 and the heat output is higher during the period 08:00–19:00, due to the increase in the desired indoor temperature and thus the increased heat demand, which are illustrated in Fig. 7(h) and (g), respectively.

Fig. 7(e) shows the COP. When no power constraints are considered the COP is nearly constant. As defined in (4) and (5), COP indicates the proportion between the heat supply from the LTDH network and the power consumption of the heat pump for a given heat output of the heat pump. Assuming the heat output of the heat pump stays constant, a higher COP indicates a higher heat supply from the LTDH network and a lower power consumption of the heat pump, thus a higher operation cost for gas consumption from the LTDH network and a lower cost for power consumption. In Case 0, the calculated COP reflects a minimization of the sum of operation cost of gas and power while fulfilling the operational temperatures of the heat pumps. Fig. 7(f) shows the SOC of the TES. Fig. 7(g) shows the heat demand of the building, and a peak appears at 08:00, due to the increased indoor temperature [shown in Fig. 7(h)]. Moreover, the heat demand is slightly reduced at noon, due to the increased ambient temperature. Fig. 7(h) shows the indoor temperature, where the green dashed line represents the desired indoor temperature. In this case, the indoor temperature setting is constant. Since no DER or BESS is available in Case 0, the PV generation is always 0 and the SOC of BESS remains at a fictitious initial level.

B. CASE STUDY 1—IMPACT OF POWER CONSTRAINTS

The results of the analysis of Case 1 are shown in Fig. 8, where the one-day profiles of operations on building C are depicted with blue curves. It is worth noting that the results of the benchmark case (i.e., Case 0) are always depicted in orange. Fig. 8(a) and (b) shows the apparent power flowing through the transformer and the current flowing through the cable, respectively. The base load is shown in green. The third subplot shows the heat pump's active power, with the red dotted line representing the maximum power constraint derived from transformer and cable capacities, presented in (21) and (22).

Period 1, from 08:00 to 11:45, depicted in gray, indicates the time when congestion occurs, where the active power in Fig. 8(c) exceeds the maximal power constraint in Case 0. In Fig. 8(b), the current flowing the cable starts to exceed its ampacity at 08:00 in Case 0, contrary to Case 1 due to the added constraints. This is more evident from Fig. 8(c), where the active power consumption of the heat pump increases at 08:00, in correspondence with the rise in heat demand due to higher set indoor temperatures as shown in Fig. 8(h). Thus, power peaks are present in Case 0, while, in Case 1 these peaks are mitigated.

Fig. 8(d)–(f) shows the heat output of the condenser, the COP of the heat pump, and the SOC of TES, respectively, for building C in Case 1. From Fig. 8(d), it can be observed that the heat output in Case 1 is lower than in Case 0 most of the time during period 1, due to reduced active power consumption, as shown in Fig. 8(c). From Fig. 8(e), it is possible to notice increases in the heat pump's COP in the test case during the congestion period. As presented in (4) and (5), COP indicates the ratio between the thermal supply from the LTDH network and the power consumption for the thermal output of the heat pump. Thus, a higher COP indicates a higher ratio of the heat supply from the LTDH network for the heat output of the heat pump. The COP is increased, by providing more heat through the LTDH network, to compensate for the decrease in heat output caused by the power consumption limitations. It is worth noting that a higher COP does not indicate a higher heat output of the heat pump. As depicted in Fig. 8, there are some periods when the COP increases but the heat output of the heat pump decreases. A higher COP indicates that the heat pump operates more efficiently, but does not imply that the whole system operates more efficiently. As defined in (31), the system operates in the most efficient range when the operation leads to minimal costs. However, the increase in COP leads to an increase in the gas volume consumed by the LTDH network and thus the operational cost. As defined in (6), to increase the COP, the return temperature $T^{*}_{\text{evap,out},t}$ from the heat pump to the LTDH network needs to be increased. This requires an increase in

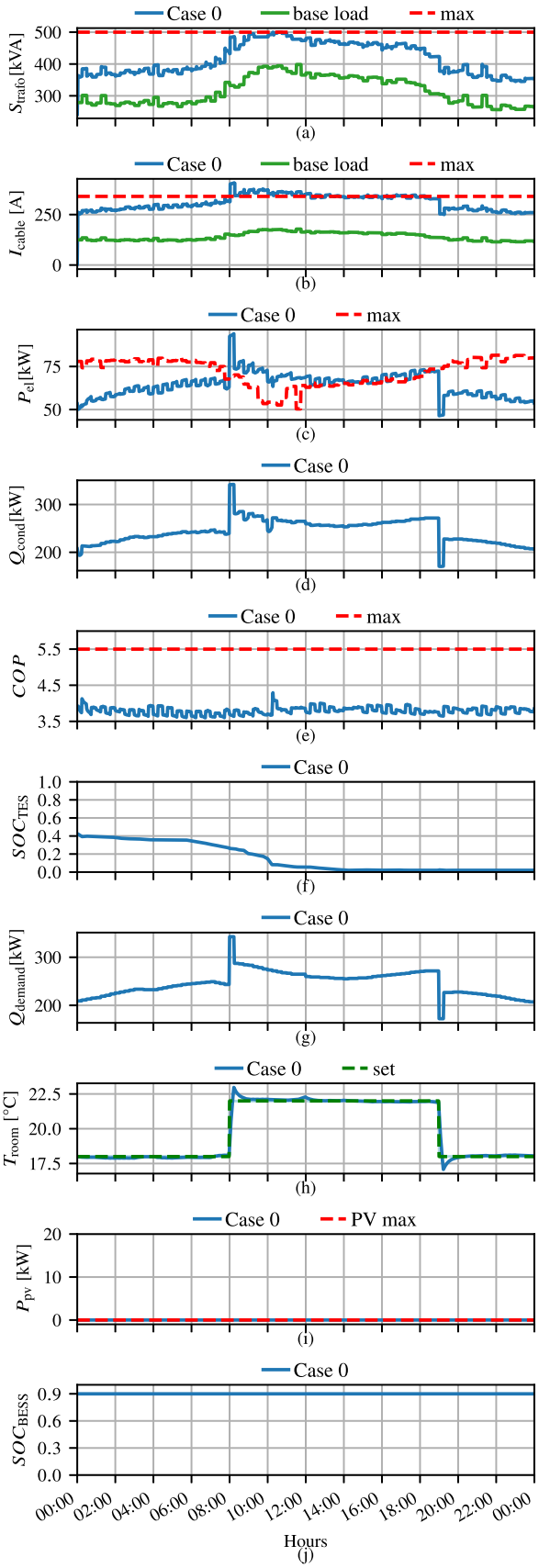

FIGURE 7. Case 0, operational states of the heat pump system in building C.

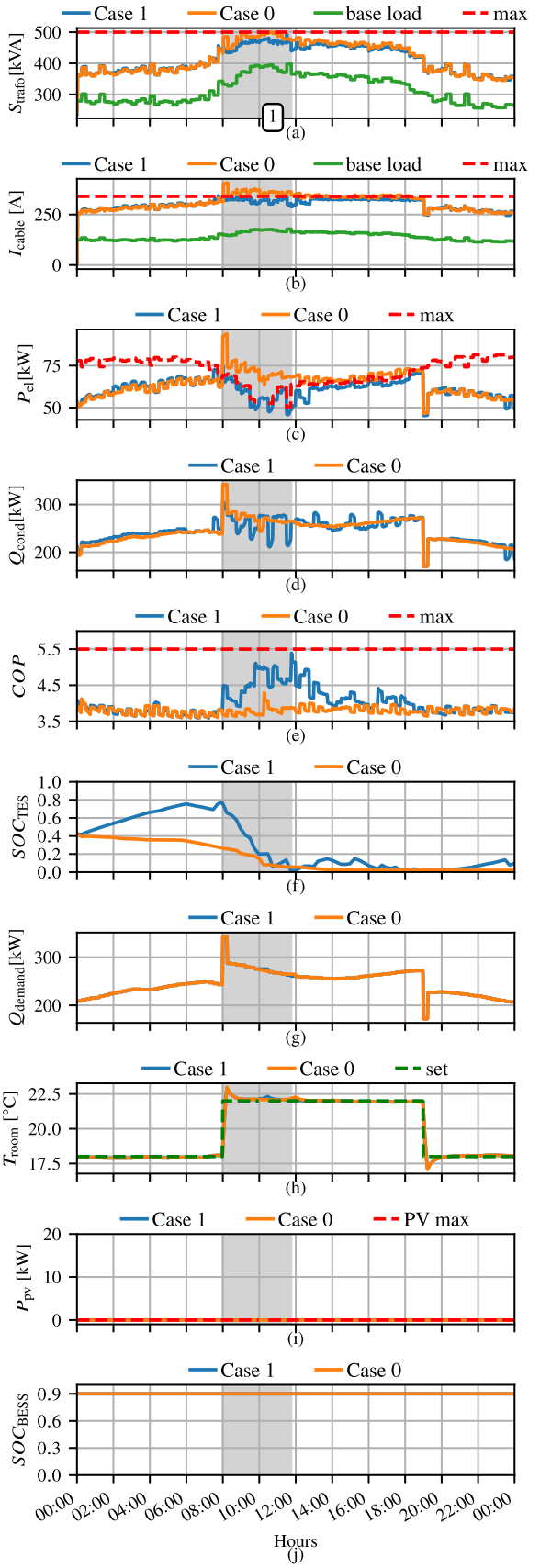

FIGURE 8. Case 1, operational states of the heat pump system in building C.

TABLE 4 Comparison of Results Between Test Cases and Case 0

Name	Case 1	Case 2	Case 3	Case 4
Benchmark	Case 0	Case 0	Case 0	Case 0
Relative gas consumption	506%	256%	287%	135%
Relative electricity supply from the grid	97.8%	96.1%	97.7%	96.1%
Relative total electricity consumption (24 h)	97.8%	99.3%	97.7%	99.2%
Relative heat pump electricity consumption (08:00-19:00)	87.5%	95.3%	87.7%	95%
Relative operation cost	161%	126%	128%	109%

the supply temperature $T^*_{\text{evap,in},t}$ and a higher mass flow rate $m_{\text{evap,in}}$ from the LTDH network, which implies that more heat is transferred to the heat pump and thus a higher gas consumption is required. This is also shown in the results of Case 0 where, in Fig. 7(e), there is no need to increase the COP up to the maximum allowed value to ensure the most efficient operation. Instead, in Case 1 and Case 2, the COP has to be increased to fulfill the power constraints while meeting the heat demand. To avoid confusion, it should be noted that when referring to the heat supply from the LTDH network, this specifically means the heat provided by the network to the evaporator of the heat pump. This definition is consistently applied in all subsequent mentions throughout this discussion.

To achieve an increase in the COP, the supply water temperature increases, resulting in a 406% increase in consumption by the gas boiler in Case 1 compared to Case 0. It is worth noting that Case 0 represents an ideal scenario, without any power consumption constraints on the heat pumps. This comparison highlights a significant increase in gas consumption when transitioning from an idealized model to a more realistic scenario that incorporates power consumption constraints for heat pumps. The comparison of the gas consumption between Case 0 and other cases is listed in Table 4.

In Fig. 8(f), thanks to the 12 h prediction period as indicated in (1), the TES in Case 1 starts to precharge at 00:00, before the grid congestion at 08:00. Contrarily, in Case 0, no pre-charging is observed. Notably, after the congestion period, the TES does not recharge immediately, due to the absence of excess waste heat or further congestion forecasted in the considered scenario. However, it starts to charge slowly at the end of the day, likely because of the congestion forecasts for the next day.

C. CASE STUDY 2—IMPACT OF DER

In Case 2, the focus is on the presence of PV and BESS. Fig. 9(a) and (b) shows the apparent power flowing through the transformer and the current flowing through the cable, respectively. Fig. 9(c) shows the active power consumption of the heat pump. The red dotted line shows the maximum active power, considering the base load, transformer capacity, and cable ampacity. This represents the maximal available active power in Case 1. The black dashed line represents the maximum active power, which includes the base load, transformer, and cable capacity, as well as the maximal PV

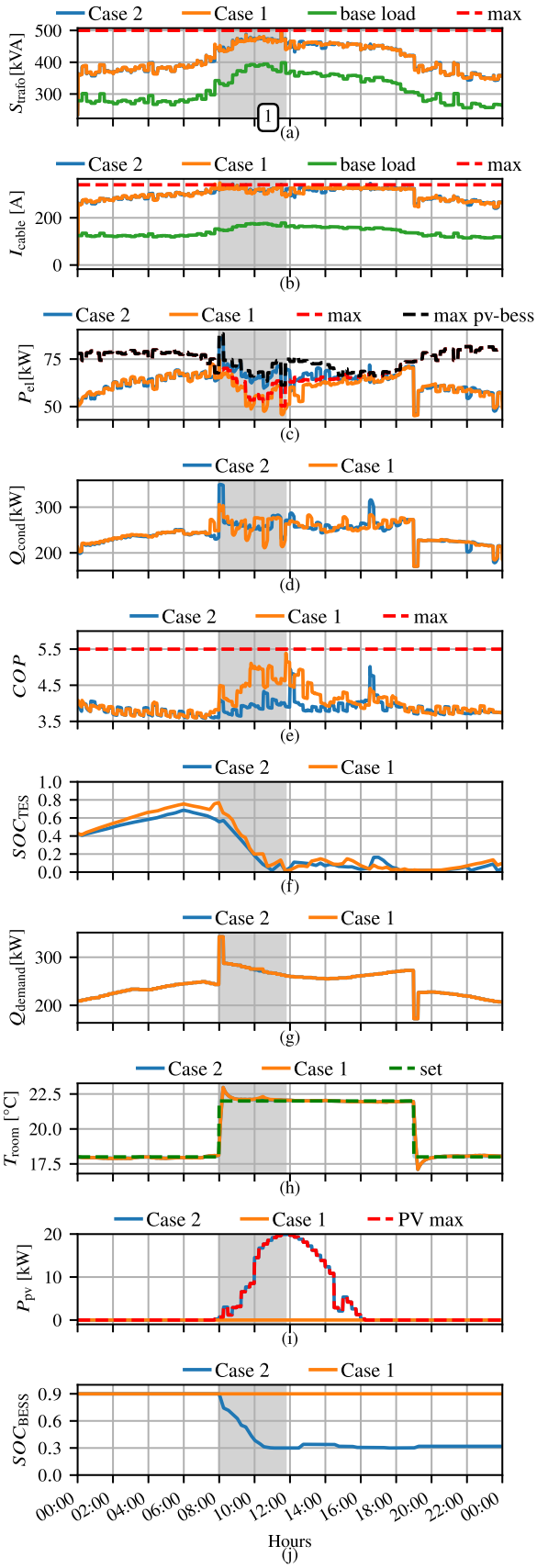

FIGURE 9. Case 2, operational states of the heat pump system in building C.

generation and battery discharge, which denotes the maximal active power in Case 2. During period 1, from 08:00 until 11:45, although the active power consumption in Case 2 is significantly higher than in Case 1, the apparent power and the cable current, shown in Fig. 9(a) and (b), respectively, remains nearly identical between Case 1 and Case 2, because of the supplementary power from the PV-BESS system. It is worth noting that the results in Fig. 9(a) and (b) show the power supply from the grid and the corresponding current consumption, respectively. In Case 2, as well as in Case 4 where the DERs are included, the BESS is assumed to be charged before the beginning of the simulation period. The PV is directly connected to the building (secondary side of the 10/0.4 kV transformer) and, in principle, this should be visible as a reduction of the power flowing through the transformer. At the same time, the MPC takes advantage of the null price associated with the PV generation by reducing the COP of the heat pump, increasing its electricity consumption, and reducing the heat absorbed by the heating grid and so the gas cost. Compared to Case 1, a peak of the heat output in Fig. 9(d) is observed in Case 2 at 08:00, when the indoor temperature is increased [shown in Fig. 9(h)]. The peak of the heat output in Case 2 is not shaved, since the peak of the heat pump's power consumption in Case 2 is not shaved, as shown in Fig. 9(c). The DERs provide the power to the heat pump when the power supply from the power grid is limited. In Case 1, the heat pump is only supplied by the power grid and the peak has to be shaved when the power grid supply is limited.

In Fig. 9(e), Case 2 shows a significantly lower COP between 08:00 and 12:00, compared to Case 1. This is attributed to the supplementary power supplied by the DERs. There is less reduced power needed to compensate for decreased heat output with heat flow from the LTDH network. Consequently, in this interval, Case 2 shows a lower COP than Case 1. The thermal constraints are considered in all cases, as shown in Table 3. Therefore, although the COP in Case 2 is reduced with respect to Case 1, it still fulfills the thermal constraints. In particular, in Case 2, thanks to the additional supply from the DERs, the COP is reduced to decrease the operational costs. As discussed in Section VI-B, when the power consumption of the heat pump is constrained, the heat transferred from the LTDH network is increased, to ensure sufficient heat supply to the buildings. Consequently, the COP is increased. In this case, the power constraints on the heat pumps are relaxed, due to the additional supply from the DERs, and thus the heat supply from the LTDH network can be reduced.

Fig. 9(f) illustrates the SOC of the TES. In both cases, the TES is heavily discharged from 08:00 to around 11:00. Notably, as shown in Fig. 9(c), despite the additional supply from the DERs, the active power consumption remains constrained. This is evident as the active power consumption (the blue line) closely aligns with the maximal allowed active power (the black dotted line). Consequently, in Fig. 9(f) a significant discharge of the TES in Case 2 is still observed during this period. Fig. 9(g) shows the heat demand of the building in Case 2. Since the indoor temperature is fixed in Case 2, the heat demands in Case 2 and Case 1 are the same. Fig. 9(h) shows the indoor temperature. Since the indoor temperature in Case 2 is set to be fixed, the result follows the desired temperature.

Fig. 9(i) and (j) shows the PV generation and the BESS SOC, respectively. The BESS discharges from 08:00 until approximately 10:00, a period during which the PV generation remains low, and the BESS primarily compensates for the reduced power supply from the grid to the heat pump. After 10:00, as the BESS reaches its minimal SOC, the PV generation becomes the primary power source for the heat pump to compensate for the reduced grid supply. It is worth noticing that no supply from the DERs is assumed in Case 1, thus there is no PV generation, and the SOC of the BESS in Case 1 remains at its initial level.

The observed differences between Case 2 and Case 1 indicate that DERs can be used to compensate for the limits on the maximum consumption of the heat pumps, without significantly increasing the heat supply from the LTDH network. Benefiting from the lower COP, the relative gas consumption in Case 2 is significantly lower compared to Case 1, leading to a significant decrease in operation cost, as indicated in Table 4. Furthermore, thanks to the supplementary supply from the DER, the electricity supply from the grid is lower, although the electricity consumption of the total loads as well as the heat pump is higher in Case 2, compared to Case 1, as indicated in Table 4.

D. CASE STUDY 3—IMPACT OF INDOOR TEMPERATURE

In Fig. 10, the profiles of operations on building C based on the results of Case 3 are depicted with blue curves, with particular emphasis on the information associated with the thermal domain.

In particular, in Fig. 10(h), the indoor temperature inside the building is shown. The region marked in light blue illustrates the maximum permissible deviation of indoor temperature with respect to the nominal one, $22 \pm 2\ ^{\circ}\mathrm{C}$.

Fig. 10(c) shows that for both Case 3 and Case 1, the heat pump power consumption is curtailed. To alleviate the congestion, the COP in both Case 3 and Case 1 is increased as shown in Fig. 10(e). Moreover, by looking at Fig. 10(h), a decrease in the temperature of the building can be observed during the congestion period, especially from 08:00 to 12:00. As a result, the heat demand in Fig. 10(g) is lower for most of the time during this period. It can be observed that at 08:00, a demand peak is shown in Case 1, due to the temperature increase in the building. Instead, in Case 3, the indoor temperature is reduced and the peak is shaved. Benefiting from the flexibility of the indoor temperature, although the COP in both scenarios is increased during the congestion period, the COP in Fig. 10(e) is often lower in Case 3 than in Case 1 during the congestion period. In Case 3, the relative gas consumption with respect to Case 0 is increased by 187%, as indicated in Table 4. Such a result is significantly lower than that in Case 1 but slightly higher than the increase in Case 2. Fig. 10(f) shows the usage of TES in Case 3, which is similar to that

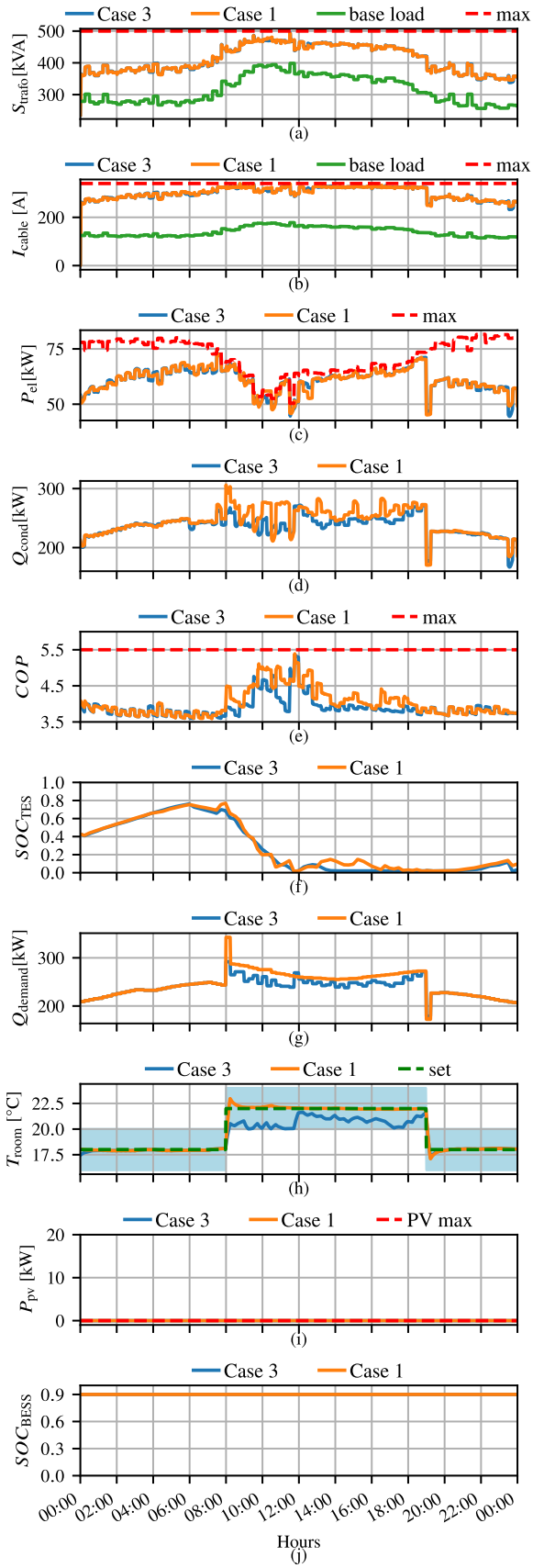

FIGURE 10. Case 3, operational response of the heat pump system in building C.

in Case 1. It is worth noting that the TES helps mitigate the grid congestion by precharging before the congestion occurs. Thus, since precharging the TES still requires the heat pump, the power consumption as well as the heat absorbed from the heating grid are increased in the period before the congestion occurs. The thermal energy stored in the TES is then used during the congestion.

E. CASE STUDY 4—IMPACT OF ALL FACTORS

Fig. 11 shows the operational states of building C, considering both the supply from the DERs and the flexibility of the indoor temperature. The benchmark case is Case 1. Because of the flexibility from both the DERs and the indoor temperature, in Case 4, the COP in Fig. 11(e) is lower and the TES in Fig. 11(f) is less discharged before 08:00, when the congestion starts. Consequently, the relative gas consumption in Case 4 to Case 0 rises by only 35%, which is substantially less than the increases in Case 1, Case 2, and Case 3.

As underlined in Case 2, from 08:00 to 10:00, the supply from the BESS [Fig. 11(j)] primarily compensates for the reduced grid supply. However, due to the flexibility of the indoor temperature, which was not considered in Case 2, the BESS is less discharged in Case 4. As a result, the temperature in Fig. 11(h) is slightly lower than the set temperature from 08:00 to 10:00. An intensive discharge of the TES is observed in Fig. 11(f) between 08:00 and 11:00. This occurs since, to overcome the congestion, in the formulation of the MPC the usage of the TES has a higher priority than lowering the indoor temperature. It is worth recalling that the priority of each action is defined by the penalties of the TES usage and thermal discomfort in the objective function.

Compared to Case 3, where no supply from DERs is considered, the temperature within the rooms of the building in Case 4 during the congestion period (08:00–19:00) is closer to the set temperature. This is because, for congestion mitigation, the usage of the DERs has a higher priority than adjusting the indoor temperature. In addition, since Case 4 utilizes both the extra supply from the DERs and the flexibility of temperature within the rooms of the building, during the congestion period, a lower COP can be observed in Fig. 11(e), as well as a slightly less precharging of TES in Fig. 11(f), compared to Case 2 and Case 3.

Finally, to further underline the impact that the various factors mentioned above have on the system operation, in Table 4, the comparison between Case 0 and other cases is summarized for each case study. Case 0 is considered as the reference for the comparison since this is the base case, where the power consumption of the heat pumps is not limited. In particular, the table presents the gas consumption, the electricity supply from the grid, the total electricity consumption over the entire simulation period, the electricity consumption of the heat pumps during the congestion period, and the overall operation cost. The gas consumption is compared to highlight the impact of power constraints on the operation of the thermal system, as well as how the activation of flexible measures in the coupled power and heating system helps mitigate the

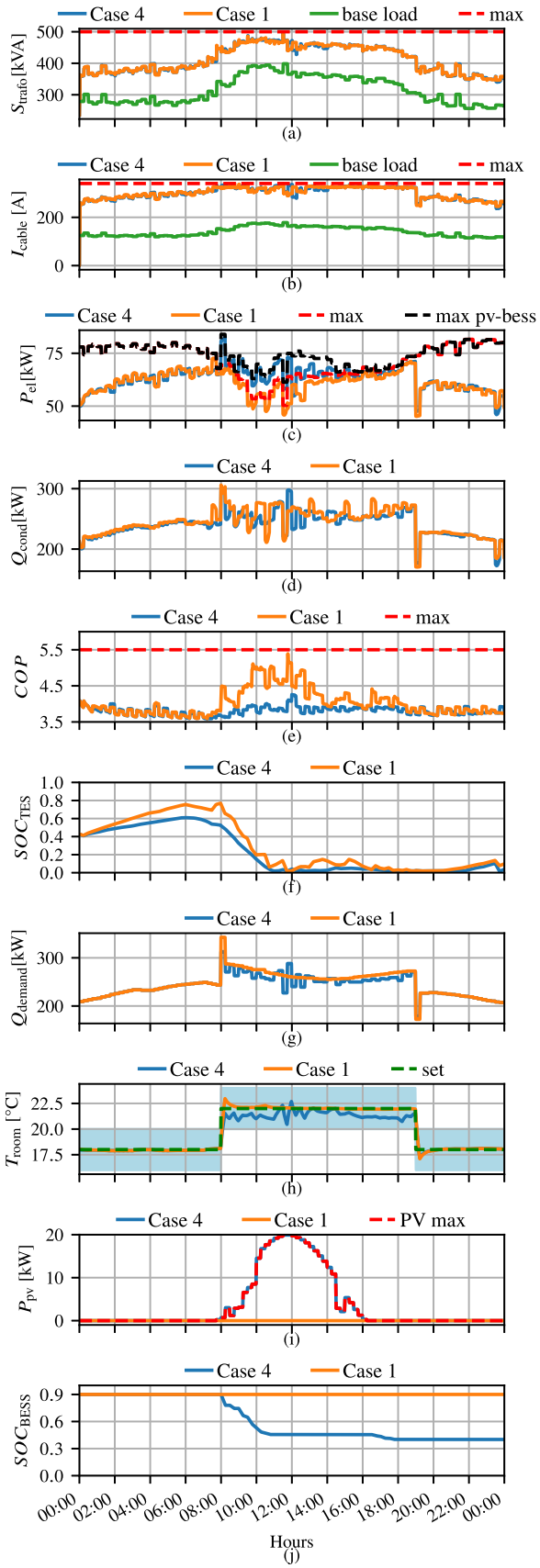

FIGURE 11. **Case 4, operational response of the heat pump system in building C.**

impacts of the power constraints. The entries related to electricity consumption and supply aim to show the impacts of the power constraints and the integration of the DERs. Finally, the operation cost, including the power and gas expenditures, shows the economic impacts of the power constraints, the DERs, and the flexible indoor temperature settings.

When considering the power grid constraints, the total electricity consumption in Case 1 is 97.8% of that in Case 0, and the power consumption of the heat pump during the congestion period (08:00-19:00) is 87.5% of that in Case 0. Compared to Case 0, the total electricity consumption in Case 1 is reduced by 2.2%, while the power consumption of the heat pump during the congestion period is decreased by 12.5%. However, to meet the heat demand when the power consumption is constrained, both the gas consumption and the operational costs are significantly increased: the gas consumption and the operation cost in Case 1 are 506% and 161% of the corresponding values in Case 0, respectively. In Case 2, with the additional supply from the DERs, the constraints on the heat pump's electricity consumption are relaxed. Thus, the heat pump's electricity consumption is increased, with a consequent increase in the total electricity consumption. Although these consumptions are increased, the power supply from the grid is decreased compared to Case 1, due to the additional supply from the DERs. Consequently, the heat supply from the LTDH network could be reduced, and the gas consumption and operational costs are lower than those in Case 1. The flexibility of the indoor temperature in Case 3, without DERs, does not bring a significant reduction in the power supply from the grid, or the consumption, compared to Case 1. However, the gas consumption and operational costs are significantly reduced. This is because the adjustable indoor temperature is exploited to reduce the heat supply from the LTDH network by reducing the heat demand. Thus, the integration of both the DERs and the adjustable indoor temperature in Case 4 contributes to the further reduction in gas consumption compared to Case 2 and Case 3, while satisfying the power grid constraints. As indicated in Table 4, compared to Case 4, the absence of DER in Case 3 results in a higher electricity supply from the grid and higher gas consumption. Consequently, the operational cost in Case 3 is higher than that in Case 4.

In the considered framework, the gas consumption must be increased, when including the power constraints. This is because the limits imposed on the power consumption of the heat pumps must be compensated by an increase of thermal energy supplied to the heat pump, so an increase in external gas consumption. By looking at this comparison, it is evident that the additional flexibility provided by the DERs or the variable indoor temperature plays a key role in reducing the usage of external gas supply. In particular, the best results can be obtained by considering both factors simultaneously.

VII. CONCLUSION

This article presents an MPC for a LTDH system equipped with heat pumps, validated within a HIL cosimulation

environment. The MPC aims to enhance the flexibility of the heat pumps in operations while taking into consideration power supply constraints during congestion periods. This is achieved by incorporating a central district heating network, TES, DERs (i.e., PVs and BESSs), and flexible indoor temperatures. Within the HIL cosimulation setup, low-level controls at the heat pump level have been developed and validated, considering the accessibility of actuators in the real system and ensuring a realistic simulation of real-world conditions. By strategically precharging the TES before high-demand periods, and increasing the COP, the power consumption of heat pumps is reduced without sacrificing the capability to provide sufficient heat to the consumers. Furthermore, the integration of DERs like PVs and BESSs, in combination with the flexibility of the indoor temperature within the building helps mitigate the congestion and reduce the pre-charging of the TES as well as the gas consumption used to compensate for the heat output decrease. In particular, compared to the case where no power grid constraints are considered, when the additional supply from DERs in the building is not included the power consumption of the heat pumps during congestion periods must be reduced to 87.5% and 87.7% for cases without and with a flexible indoor temperature setting, respectively. With DERs, thanks to the maximization of self-consumption within the building, the power consumption of the heat pumps is limited to 95.3% when no adjustable indoor temperature is considered and 95% with a flexible indoor temperature, but the electricity supply from the grid is the lowest.

The presented work can be extended with further studies: i) scaling the LTDH network and analyzing the MPC's capability to provide ancillary services to the power grid; ii) comparing the proposed MPC with other regulation methods to quantify its robustness, optimality of control actions, and performance when considering uncertainties.

ACKNOWLEDGMENT

Views and opinions expressed are however those of the author(s) only and do not necessarily reflect those of the European Union or CINEA. Neither the European Union nor the granting authority can be held responsible for them.

REFERENCES

[1] O. Ruhnau, S. Bannik, S. Otten, A. Praktiknjo, and M. Robinius, "Direct or indirect electrification? A review of heat generation and road transport decarbonisation scenarios for Germany 2050,"*Energy*, vol. 166, pp. 989–999, 2019. [Online]. Available: https://www.sciencedirect.com/science/article/pii/S0360544218321042

[2] M. Schlemminger, T. Ohrdes, E. Schneider, and M. Knoop, "Dataset on electrical single-family house and heat pump load profiles in Germany," *Sci. Data*, vol. 9, 2022, Art. no. 56.

[3] W. Zheng, H. Lu, M. Zhang, Q. Wu, Y. Hou, and J. Zhu, "Distributed energy management of multi-entity integrated electricity and heat systems: A review of architectures, optimization algorithms, and prospects," *IEEE Trans. Smart Grid*, vol. 15, no. 2, pp. 1544–1561, Mar. 2024.

[4] Z. E. Lee, Q. Sun, Z. Ma, J. Wang, J. S. MacDonald, and K. M. Zhang, "Providing grid services with heat pumps: A review," *ASME J. Eng. Sustain. Buildings Cities*, vol. 1, no. 1, 2020, Art. no. 011007, doi: 10.1115/1.4045819.

[5] A. Afram and F. Janabi-Sharifi, "Theory and applications of HVAC control systems–A review of model predictive control (MPC)," *Building Environ.*, vol. 72, pp. 343–355, 2014.

[6] B. van der Holst et al., "A quantification method for the potential downward flexibility of full-electric heat pumps during congestion events," in *Proc. IEEE Belgrade PowerTech*, 2023, pp. 1–6.

[7] C. Srithapon and D. Månsson, "Predictive control and coordination for energy community flexibility with electric vehicles, heat pumps and thermal energy storage," *Appl. Energy*, vol. 347, 2023, Art. no. 121500.

[8] X. Wang, L. Liang, X. Zhang, and H. Sun, "Distributed real-time temperature and energy control of energy efficient buildings via geothermal heat pumps," *CSEE J. Power Energy Syst.*, vol. 9, no. 6, pp. 2289–2300, 2023.

[9] M. Taylor, S. Long, O. Marjanovic, and A. Parisio, "Model predictive control of smart districts with fifth generation heating and cooling networks," *IEEE Trans. Energy Convers.*, vol. 36, no. 4, pp. 2659–2669, Dec. 2021.

[10] M. Taylor, O. Marjanovic, and A. Parisio, "Decentralized supervisory control of networked multienergy buildings," *IEEE Trans. Control Syst. Technol.*, vol. 32, no. 3, pp. 945–959, May 2024.

[11] D. Fischer and H. Madani, "On heat pumps in smart grids: A review," *Renewable Sustain. Energy Rev.*, vol. 70, pp. 342–357, 2017.

[12] B. Chen et al., "Energy-circuit-based integrated energy management system: Theory, implementation, and application," *Proc. IEEE*, vol. 110, no. 12, pp. 1897–1926, Dec. 2022.

[13] H. Cai and P. Heer, "Experimental implementation of an emission-aware prosumer with online flexibility quantification and provision," *Sustain. Cities Soc.*, vol. 111, 2024, Art. no. 105531.

[14] M. Chamana et al., "Buildings participation in resilience enhancement of community microgrids: Synergy between microgrid and building management systems," *IEEE Access*, vol. 10, pp. 100922–100938, 2022.

[15] D. Hering, M. E. Cansev, E. Tamassia, A. Xhonneux, and D. Müller, "Temperature control of a low-temperature district heating network with model predictive control and mixed-integer quadratically constrained programming," *Energy*, vol. 224, 2021, Art. no. 120140.

[16] D. Liu, D. Hering, D. Carta, A. Xhonneux, D. Müller, and A. Benigni, "A hardware-in-the-loop co-simulation of multi-modal energy system for control validation," in *Proc. 47th Annu. Conf. IEEE Ind. Electron. Soc.*, 2021, pp. 1–6.

[17] Forschungszentrum Jülich, "Forschungszentrum jülich. Living lab energy campus (LLEC)," Accessed: Nov. 4, 2024. [Online]. Available: https://www.fz-juelich.de/llec

[18] European Commission, "Energy communities," Accessed: Nov. 4, 2024. [Online]. Available: https://energy.ec.europa.eu/topics/markets-and-consumers/energy-consumers-and-prosumers/energy-communities_en

[19] D. Müller, M. Lauster, A. Constantin, M. Fuchs, and P. Remmen, "AixLib—An open-source modelica library within the IEA-EBC annex 60 framework," in *Proc. BauSim Conf., 6th Conf. IBPSA-Germany Austria*, ser. BauSim Conference, 2016, pp. 3–9.

[20] D. Hering, A. Xhonneux, and D. Mueller, "Economic and ecologic evaluation of low temperature waste heat integration into existing district heating," in *Proc. 16th Int. Conf. Int. Building Perform. Simul. Assoc.*, 2019, pp. 3250–3257.

[21] D. Hering, M. R. Faller, A. Xhonneux, and D. Müller, "Operational optimization of a 4th generation district heating network with mixed integer quadratically constrained programming," *Energy*, vol. 250, 2022, Art. no. 123766.

[22] L. Wang, *Model Predictive Control System Design and Implementation Using MATLAB*, 1st ed. Berlin, Germany: Springer, 2009.

[23] Viessmann Climate Solutions SE, "Vitocal 350-ht pro technical guide," Accessed: Dec. 10, 2023. [Online]. Available: https://www.kekelit.co.nz/wp-content/uploads/2021/03/Vitocal-350-HT-Pro-instituteTechnical-Guide.pdf

[24] P. Remmen, M. Lauster, M. Mans, M. Fuchs, T. Osterhage, and D. Mueller, "Teaser: An open tool for urban energy modelling of building stocks," *J. Building Perform. Simul.*, vol. 11, pp. 1–15, 2017.

[25] D. Hering, A. Xhonneux, and D. Müller, "Design optimization of a heating network with multiple heat pumps using mixed integer quadratically constrained programming," *Energy*, vol. 226, 2021, Art. no. 120384.

[26] Gurobi Optimization, "Gurobi," Accessed: Dec. 9, 2023. [Online]. Available: https://www.gurobi.com/
[27] D. Liu, D. Carta, A. Xhonneux, D. Müller, and A. Benigni, "An MQTT gateway for HIL testing of energy systems," in *Proc. 48th Annu. Conf. IEEE Ind. Electron. Soc.*, 2022, pp. 1–6.
[28] S. Gros, M. Zanon, R. Quirynen, A. Bemporad, and M. Diehl, "From linear to nonlinear MPC: Bridging the gap via the real-time iteration," *Int. J. Control*, vol. 93, pp. 1–19, 2016.
[29] W.-H. Chen, D. J. Ballance, and J. O'Reilly, "Model predictive control of nonlinear systems: Computational burden and stability," *IEE Proc.-Control Theory Appl.*, vol. 147, no. 4, pp. 387–394, 2000.
[30] M. A. K. Gomaa, O. De Silva, G. K. I. Mann, and R. G. Gosine, "Computationally efficient stability-based nonlinear model predictive control design for quadrotor aerial vehicles," *IEEE Trans. Control Syst. Technol.*, vol. 31, no. 2, pp. 615–630, Mar. 2023.

DIRAN LIU (Member, IEEE) received the B.Sc. and M.Sc. degrees in energy and environment system engineering from Shandong University, Jinan, China, and in energy science and engineering from Technical University of Darmstadt, Darmstadt, Germany, in 2017 and 2020, respectively. She is currently working toward the Ph.D. degree in mechanical engineering with the "Institute of Climate and Energy Systems: Energy Systems Engineering, ICE-1," of Forschungszentrum Jülich, Jülich, Germany.

DANIELE CARTA (Member, IEEE) received the B.Sc. and M.Sc. degrees in electrical engineering and the Ph.D. degree in electrical engineering from the University of Cagliari, Cagliari, Italy, in 2013, 2016, and 2020, respectively.

He is currently the Group Leader of the "Control Solution" Group with the "Institute of Climate and Energy Systems: Energy Systems Engineering, ICE-1," of Forschungszentrum Jülich, Jülich, Germany.

ANDRÉ XHONNEUX received the Diploma degree in mechanical engineering and the Ph.D. degree in mechanical engineering from RWTH Aachen University, Aachen, Germany, in 2008 and 2015, respectively.

He is the Department Leader of the "Buildings and Districts" Group, "Institute of Climate and Energy Systems: Energy Systems Engineering, ICE-1," of Forschungszentrum Jülich, Jülich, Germany.

DIRK MÜLLER received the B.Sc. degree in mechanical engineering from Thayer School of Engineering at Dartmouth, Hanover, NH, USA, in 1994 and the Diploma in mechanical engineering from RWTH Aachen University, Aachen, Germany, in 1995. He received Dr.-Ing. degree in mechanical engineering from RWTH Aachen University.

From 2003 to 2007, he was a Full Professor (W4) and the Director of the Hermann-Rietschel-Institute, Technical University of Berlin. He is currently the Director of the "Institute of Climate and Energy Systems: Energy Systems Engineering, ICE-1," of Forschungszentrum Jülich (since 2017) and a Full Professor (W3) and the Director of the Institute of Institute for Energy Efficient Buildings and Indoor Climate at E.ON Energy Research Center, RWTH Aachen University (since 2007).

ANDREA BENIGNI (Senior Member, IEEE) received the B.Sc. and M.Sc. degrees in electrical engineering from Politecnico di Milano, Milano, Italy, in 2005 and 2008, respectively, and the Ph.D. degree in electrical engineering from RWTH-Aachen University, Aachen, Germany, in 2013.

From 2014 to 2019, he was an Assistant Professor with the Department of Electrical Engineering, University of South Carolina, Columbia, SC, USA. Since 2019, he has been a Full Professor with RWTH-Aachen and the Director of the "Institute of Climate and Energy Systems: Energy Systems Engineering, ICE-1," of Forschungszentrum Jülich, Jülich, Germany.